ACS APPLIED MATERIALS & INTERFACES

Biological and Medical Applications of Materials and Interfaces

Intrinsically Cancer-Mitochondria-Targeted Thermally Activated Delayed Fluorescence Nanoparticles for Two-Photon Activated Fluorescence Imaging and Photodynamic Therapy

Jinfeng Zhang, Fang Fang, Bin Liu, Ji-Hua Tan, Wen-Cheng Chen, Zelin Zhu, Yi Yuan, Yingpeng Wan, Xiao Cui, Shengliang Li, Qing-Xiao Tong, Junfang Zhao, Xiangmin Meng, and Chun-Sing Lee

ACS Appl. Mater. Interfaces, **Just Accepted Manuscript** • DOI: 10.1021/acsami.9b14552 • Publication Date (Web): 11 Oct 2019

	Physics and Chemistry; City University of Hong Kong, Joint Laboratory of Nano-organic Functional Materials and Devices (TIPC and CityU) Meng, Xiangmin; Chinese Academy of Sciences, Technical Institute of Physics and Chemistry; City University of Hong Kong, Joint Laboratory of Nano-organic Functional Materials and Devices (TIPC and CityU) Lee, Chun-Sing; City University of Hong Kong, Center of Super-Diamond and Advanced Films (COSDAF) & Department of Chemistry; City University of Hong Kong, Joint Laboratory of Nano-organic Functional Materials and Devices (TIPC and CityU)

Intrinsically Cancer-Mitochondria-Targeted Thermally Activated Delayed Fluorescence Nanoparticles for Two-Photon Activated Fluorescence Imaging and Photodynamic Therapy

Jinfeng Zhang †, Fang Fang †, Bin Liu ǂ,§, Ji-Hua Tan #,ǁ, Wen-Cheng Chen #,ǁ, Zelin Zhu #,ǁ, Yi Yuan #,ǁ, Yingpeng Wan #,ǁ, Xiao Cui #,ǁ, Shengliang Li #,ǁ,, Qing-Xiao Tong §, Junfang Zhao Δ,ǁ, Xiang-Min Meng Δ,ǁ and Chun-Sing Lee #,,ǁ**

† Key Laboratory of Molecular Medicine and Biotherapy, School of Life Sciences, Beijing Institute of Technology, Beijing, P. R. China

ǂ School of Science, Westlake Institute for Advanced Study, Westlake University, 18 Shilongshan Road, Hangzhou, P. R. China, Department of Physics, Fudan University, Shanghai, P. R. China

§ Department of Chemistry and Key Laboratory for Preparation and Application of Ordered Structural Materials of Guangdong Province, Shantou University, 243 University Road, Shantou, Guangdong 515063, P.R. China

Center of Super-Diamond and Advanced Films (COSDAF) & Department of Chemistry, City University of Hong Kong, 83 Tat Chee Avenue, Kowloon, Hong Kong SAR, P. R. China

E-mail: lishengliang@iccas.ac.cn; apcslee@cityu.edu.hk

ǁ Joint Laboratory of Nano-organic Functional Materials and Devices (TIPC and CityU), City University of Hong Kong, Hong Kong SAR, P. R. China

Δ Technical Institute of Physics and Chemistry, Chinese Academy of Sciences, Beijing 100190, China

KEYWORDS: *cancer-mitochondria-targeted, thermally activated delayed fluorescence (TADF), two-photon activated, fluorescence imaging, photodynamic therapy,*

ABSTRACT: A recent breakthrough in the discovery of thermally activated delayed fluorescence (TADF) emitters which characterized with small single-triplet energy offsets (ΔE_{ST}) offers a wealth of new opportunities to exploit high-performance metal-free PSs. In this report, two intrinsically cancer-mitochondria-targeted TADF emitters based nanoparticles (TADF NPs) have been developed for two-photon activated photodynamic therapy (PDT) and fluorescence imaging. The as-prepared

TADF NPs integrate the merits of 1) high $^1O_2$ quantum yield of 52%; 2) sufficient near-infrared (NIR) light penetration depth due to two-photon activation; 3) excellent structure-inherent mitochondria-targeting capabilities without extra chemical or physical modifications, inducing remarkable endogenous mitochondria-specific ROS production and excellent cancer-cell-killing ability upon an ultralow light irradiance. We believe that the development of such intrinsically multifunctional TADF NPs stemming from a single molecule will provide new insights into exploration of novel PDT agents with strong photosensitizing ability for various biomedical applications.

1. INTRODUCTION

Photodynamic therapy (PDT) is one of the most promising modalities against cancer owing to its minimal invasiveness, good specificity, negligible drug resistance as well as excellent repeatability with relatively mild side effects.[1–9] In PDT, an optically-excited photosensitizer (PS) transfers its obtained energy to surrounding oxygen molecules to generate reactive oxygen species (ROSs), typically singlet oxygen ($^1O_2$).[3] Upon photoexcitation, the PS will first form a singlet excited state as governed by the requirement of spin conservation. Before passing its energy to the surrounding oxygen, the singlet-excited PS has to go through an intersystem crossing (ISC) to shape into a triplet-excited state. Therefore, an efficient ISC process is critical for the formation of $^1O_2$ and improvement of PDT performance.[10–13] Currently, a commonly used strategy is to introduce heavy-metal atoms into the PS molecules for enhancing spin-orbit coupling and thus ISC.[14–16] However, the inherent cytotoxicity and unsatisfactory degradability originating from these heavy-metal-containing PSs would hinder their further wide clinical translations.[10,17,18]

Fortunately, a recent breakthrough in the discovery of thermally activated delayed fluorescence (TADF) emitters in the area of organic light-emitting device (OLED) [15–22] offers a new possibility of getting high performance metal-free PSs with strong photosensitizing ability. TADF emitters are pure organic fluorescent molecules characterized with small single-triplet energy offsets (ΔE_{ST}). Particularly, such small ΔE_{ST} will lead to easily energy conversion between singlet and triplet PS and thus enabling efficient ISC. In fact, while these TADF emitters exhibit many fascinating optical properties, there have been so far only few reports on their biomedical applications which only exploit their delayed fluorescence for time-resolved luminescence imaging.[23–25] As a proof of principle, we have shown for the first time that TADF emitters can indeed be used as novel metal-free PSs for $^1O_2$ generation.[26] While this new concept for developing metal-free PDT agents is promising, $^1O_2$ quantum yield of these TADF PDT agents are so far below 15%.[26] This value is clearly much lower than the new concept should suggest in principle. On the other hand, there are still limitations in most reported PDT agents which hindered their wide clinical applications. In addition to $^1O_2$ quantum yield, enhancements in (i) optical penetration depth in body tissue, (ii) targeting to specific subcellular organelles and (iii) image-guided theranostic capability are highly desirable. More importantly, to the best of our knowledge, there has been no any single TADF based agent that can be able to concurrently address all of the above issues, which is attractive for PDT treatment and future clinical application.

In this work, we developed two intrinsically cancer-mitochondria-targeted TADF based organic nanoparticles (TADF NPs) for two-photon activated PDT and fluorescence imaging. These two TADF nanophotosensitizers combine the merits of high $^1O_2$ quantum yields, sufficient near-infrared (NIR) light penetration depth, good *in vitro* biocompatibility, two-photon activated cellular

fluorescence imaging, endogenous mitochondria-specific ROS production and excellent cancer-cell-killing ability. We believe that the development of such intrinsically multifunctional TADF based nanostructures will provide new insights into exploration of novel PDT agents for various biomedical applications.

2. EXPERIMENTAL SECTION

2.1 Materials. 9,10-anthracenedipropionicacid (ADPA), 2,7-dichlorofluorescein diacetate (DCFH-DA), 4, 6-diamidino-2-phenylindole (DAPI), Rose bengal, 4, 5-Dimethylthiazol-2-yl)-2, 5-diphenyl tetrazolium bromide (MTT) were purchased from Sigma. Dulbecco's modified Eagle's medium (DMEM, high glucose), trypsin-EDTA, Dulbecco's phosphate buffered saline (PBS, 10X, pH 7.4), penicillin-streptomycin, fetal bovine serum (FBS), 5,59,6,69-tetrachloro-1,19,3,39-tetraethylbenzimidoazolylcarbocyanino iodide (JC-1) were purchased from ThermoFisher Scientific.

2.2 Synthesis of An-TPA and An-Cz-Ph. 2-Bromoanthraquinone (2.67 mmol, 765 mg), 4-(diphenylamino)phenylboronic acid (2.67 mmol, 772 mg) or 9-phenyl-9*H*-carbazol-3-ylboronic acid (2.67 mmol, 765 mg), tetrakis-(triphenylphosphine)-palladium(0) (0.13 mmol 150 mg), 8 mL aqueous K_2CO_3 (2M), 8 mL ethanol were added into toluene (30 mL). The mixture was stirred at 120 °C for 24 h under argon atmosphere. After cooling to room temperature, the organic phase was washed with 20 mL water and extracted with dichloromethane, then was dried with anhydrous Na_2SO_4 and concentrated by rotary evaporation. Finally, column chromatography (petroleum ether: CH_2Cl_2 = 4: 1) on silica gel was used to purify the residue to obtain a red powder (An-TPA: 0.94 g/78%, An-Cz-Ph: 0.88 g/73%)

Characterization of An-TPA: ^{1}H NMR (600 MHz, $CDCl_3$) δ 8.66 (s, 1H), 8.51 (s, 1H), 8.39 (d, J = 8.1 Hz, 1H), 8.37-8.31 (m, 2H), 8.23 (d, J = 7.7 Hz, 1H), 8.15 (d, J = 8.0 Hz, 1H), 7.80 (dt, J = 14.7, 7.0 Hz, 3H), 7.64 (t, J = 7.7 Hz, 2H), 7.59 (d, J = 7.7 Hz, 2H), 7.50 (t, J = 7.8 Hz, 2H), 7.47-7.40 (m, 2H), 7.34 (t, J = 7.1 Hz, 1H). ^{13}C NMR (151 MHz, $CDCl_3$) δ [ppm]: 183.5, 183.0, 147.6, 141.3, 137.3, 134.1, 133.7, 132.2, 131.4, 130.8, 130.0, 128.1, 127.8, 127.2, 127.0, 126.5, 125.3, 124.1, 123.2, 120.5, 119.3, 110.4, 110.1. MS (ESI): m/z = 449.1 $[M]^+$.

Characterization of An-Cz-Ph: ^{1}H NMR (600 MHz, $CDCl_3$) δ 8.50 (s, 1H), 8.33 (dd, J = 10.7, 6.5 Hz, 3H), 7.98 (dd, J = 8.1, 1.4 Hz, 1H), 7.83-7.77 (m, 2H), 7.61 (d, J = 8.5 Hz, 2H), 7.29 (t, J = 7.8 Hz, 4H), 7.15 (dd, J = 8.4, 2.8 Hz, 6H), 7.08 (t, J = 7.3 Hz, 2H). ^{13}C NMR (151 MHz, $CDCl_3$) δ [ppm]: 183.4, 182.8, 148.8, 147.2, 146.3, 145.7, 134.1, 133.9, 133.7, 133.6, 131.9, 131.5, 129.4, 128.1, 128.0, 127.2, 127.2, 125.0, 123.6, 122.9. MS (ESI): m/z = 452.2 $[M + H]^+$.

2.3 Preparation of the An-TPA NPs and An-Cz-Ph NPs. An-TPA NPs and An-Cz-Ph NPs were prepared using the traditional nanoprecipitation method, in which An-TPA and An-Cz-Ph were respectively dissolved in THF with 1 mg/mL concentration. 200 μL of the above solution was quickly added into 5 mL of DI water drop by drop under energetic stirring for 10 min. Another 10 min of sonication was applied to the above-obtained solutions in order to ensuring total THF evaporation and then dispersions of the An-TPA NPs or An-Cz-Ph NPs were finally collected for further use.

2.4 Characterization of the An-TPA NPs and An-Cz-Ph NPs. Sizes and morphologies of the as-fabricated TADF NPs were characterized with both scanning electron microscopy (SEM, Philips XL-30 FEG) and transmission electron microscopy (TEM, Hitachi H-7700). Dynamic light scattering (DLS) and polydispersity index (PDI) measurements were determined by using a Malvern

Zetasizer. Optical absorption and emission spectra were individually measured with a UV-vis-NIR spectrophotometer (PE Lamda 19) and a fluorescence spectrophotometer (Cary Eclipse).

2.5 SPE and TPE cellular imaging. All cells including two cancer cell lines (A549 or Hela cancer cells) and two normal cell lines (NIH 3T3 or MCR-5 normal cells) were cultured with standard DMEM culture medium which contained 10% FBS and 1% penicillin/streptomycin in a humidified 5% CO_2 -incubator at 37 °C. For SPE cellular imaging, the assigned cells were first seeded on 6-well plates for 24 h and then the TADF NPs dispersions with final concentration of 8 μg/mL were added to each plate. After incubation for another 4 h, the treated cells were washed thoroughly and then stained with nuclei-dye DAPI for 5 min. Finally, SPE fluorescent images of the treated cells were captured by using a Nikon ECLIPSE 80i fluorescent microscope. For TPE cellular imaging, the cells were seeded on 35 mm Laser confocal petri dishes for 24 h and the TADF NPs dispersions with final concentration of 8 μg/mL were individually added to each plate. After incubation for 4 h, TPE fluorescent images of the treated cells were recorded by using a confocal laser scanning microscopy (CLSM, Leica TCS SP5) with 800 or 880 nm two-photon fs excitation.

2.6 $^1O_2$ quantum yield measurements. Production of $^1O_2$ was determined by using the disodium salt of ADPA which absorption at 378 nm would be degraded upon exposure to $^1O_2$. Rose bengal was selected as a calibration standard with $^1O_2$ quantum yield of 75% in water. 60 μL of ADPA water solution (1 mg/mL) was added into 2 mL of the TADF NPs dispersions. The mixed solutions were irradiated with a xenon lamp only passing light from 400 to 700 nm by equipping with a filter. The maximal absorption of all samples was adjusted to 0.15-0.3 OD and recorded every 30 s to obtain the decay rate of the photosensitizing process. $^1O_2$ quantum yield of the NP samples were calculated using the following formula:

$\Phi_{sample}=\Phi_{rose\ bengal}*K_{sample}*A_{rose\ bengal}/(K_{rose\ bengal}*A_{sample})$; where K_{sample} and $K_{rose\ bengal}$ are the decomposition rate constants of the disodium salt of ADPA by the TADF NPs and Rose bengal, respectively. $A_{rose\ bengal}$ and A_{sample} represent integral areas of the optical absorption bands between 400 and 700 nm by the Rose bengal and TADF NPs, respectively.

2.7 Colocalization of TADF NPs with the MitoTracker Green or LysoTracker Green. Two cancer cell lines (A549 or Hela cancer cells) and two normal cell lines (NIH 3T3 or MCR-5 normal cells) were seeded on 35 mm Laser confocal petri dishes and incubated with TADF NPs with final concentration of 8 μg/mL for 4 h. Then the treated cells were co-incubated with commercial mitochondrion-staining agent MitoTracker Green (100 nM) or lysosome-staining agent LysoTracker Green (100 nM) for 30 min. The live cells were then visualized by using a confocal laser scanning microscopy (CLSM, Leica TCS SP5)

2.8 Cytotoxicity by MTT assay. Firstly, the A549 cells were cultured in 96-well plates with standard DMEM culture medium in a humidified 5% CO_2 -incubator at 37 °C. After growing overnight, original medium were removed. Then 200 μl of DMEM medium containing TADF NPs with given concentration were added to the plates where the final concentration of these TADF NPs in the designated wells ranged from 1.25 to 20 μg/mL. After 24 h dark incubation, the cells incubated with these NPs were irradiated for 5 min with white light (400 to 700 nm) at a power density of 28 mW/cm^2. The irradiated cells were then incubated darkly for another 24 h. Subsequently, removing the original medium in each well. Afterwards, 200 μL of DMEM-MTT solution (10 % MTT stock solution) in the absence of FBS were added in each well and incubated darkly for 4 hours. After completely removing the MTT-containing medium, 200 μL of DMSO was added into each well. Cell viabilities were finally determined by using a microplate reader (BioTek Powerwave XS).

3. RESULTS AND DISCUSSION

3.1. Synthesis and Characterization of TADF Molecules. The two TADF molecules, 2-(4-(diphenylamino)phenyl)anthracene (An-TPA) and 3-(9-phenyl-9*H*-carbazol-6-yl)anthracene-9,10-dione (An-Cz-Ph) are prepared by typical Suzuki coupling reactions as shown in **Figure 1a**. Chemical structures of the An-TPA and the An-Cz-Ph were individually confirmed with $^{1}H/^{13}C$ NMR and mass spectrometric analysis. Optimized molecular geometries and frontier molecular orbital distribution calculated *via* DFT approach using B3LYP/6-31G(d) basis set with the Gaussian 09 program are displayed in **Figure 1b**. It can be found that both molecules have nonplanar conformations which will reduce intermolecular π-π stacking in solid and enable the TADF materials to exhibit good fluorescence in solid state. As shown in **Figure S1**, intense red emissions from the An-TPA and the An-Cz-Ph powders can be clearly observed while the fluorescence of a commercial green dye FITC is nearly quenched due to aggregation-caused quenching effect, which is beneficial for potential imaging application. Optimization of the singlet and triplet excited states was performed by the time-dependent DFT/B3LYP/6-31G(d) method. **Figure 1b** also displays that both molecules have well-separated HOMO and LUMO distributions which are essential for getting small ΔE_{ST} (0.17 and 0.24 eV for An-TPA and An-Cz-Ph) needed for TADF and efficient ISC for high performance PDT. It is worth noting that triphenylamine (TPA) is a more electron-rich group with strong intramolecular charge-transfer ability than N-phenylcarbazole (Cz-Ph) group. So An-TPA exhibited smaller ΔE_{ST} due to much more separated HOMO/LUMO distribution.

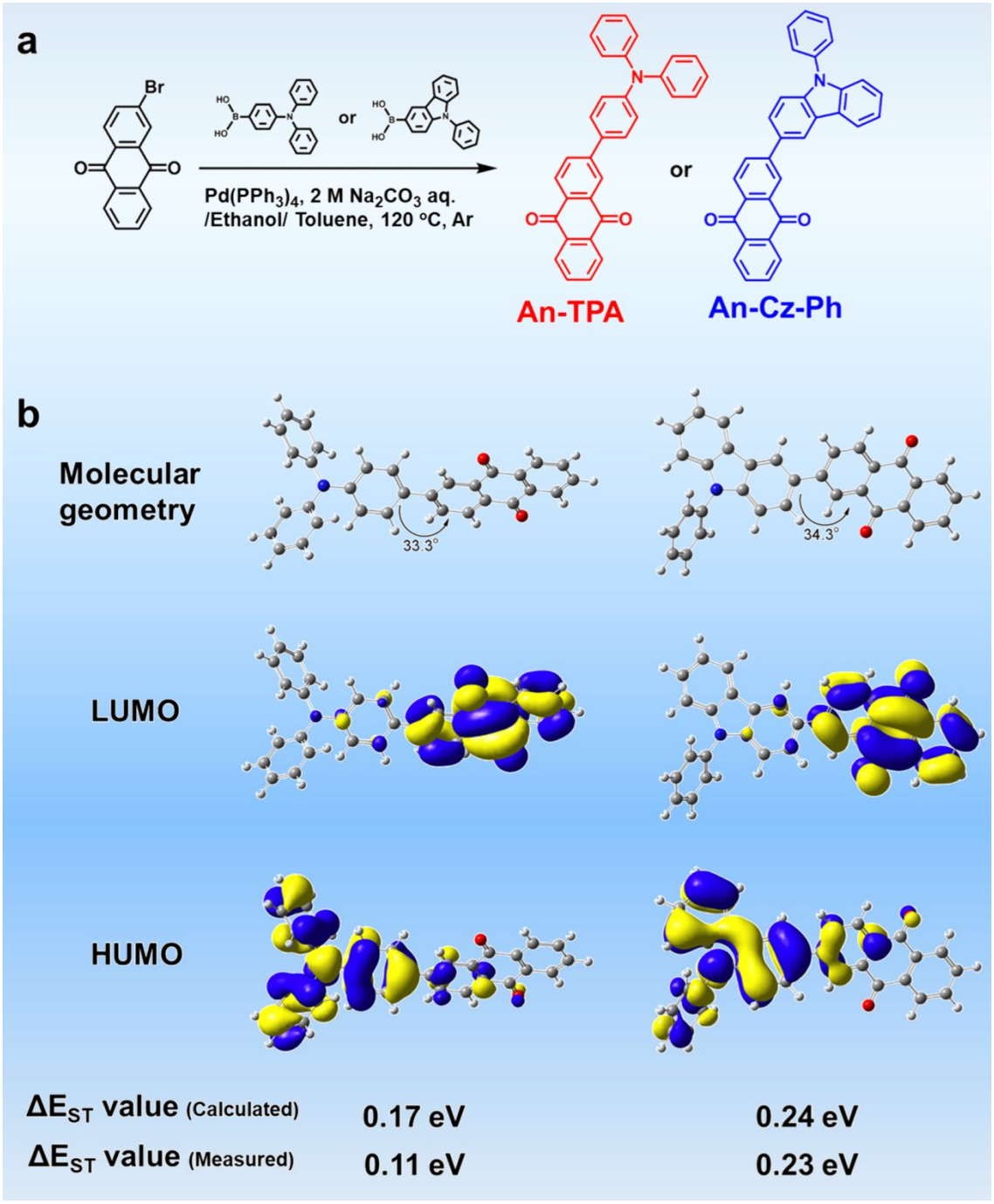

Figure 1. a) Synthetic routes for An-TPA and An-Cz-Ph; b) Molecular geometries and HOMO-LUMO distributions of An-TPA and An-Cz-Ph, which were optimized by DFT calculations.

To investigate TADF properties of An-TPA and An-Cz-Ph, spectroscopic characteristics of these molecules dissolved in 2-methyltetrahydrofuran and doped in a bis[2-(diphenylphosphino)phenyl] ether oxide (DPEPO) solid film have been measured. **Figure S2** presents the steady-state

fluorescence (measured at room temperature) and phosphorescence spectra (measured at 77 K) of the An-TPA and the An-Cz-Ph dissolved in solution. According to the difference in the onset wavelengths of fluorescence and phosphorescence spectra, ΔE_{ST} values of An-TPA and An-Cz-Ph were determined to be 0.11 eV and 0.23 eV, respectively. These experimental ΔE_{ST} values are well consistent with the calculated ones shown in **Figure 1b.** Furthermore, transient photoluminescence decay curves of the An-TPA and the An-Cz-Ph doped solid films (**Figures S2 c, d**), clearly show short and long decay components which are individually ascribed to the prompt fluorescence and delayed TADF components.[27] Besides, temperature-dependent transient photoluminescence spectra of the An-TPA and An-Cz-Ph samples further confirm the distinct TADF characteristics of An-TPA and An-Cz-Ph (**Figure S3**).

2.2. Preparation and Characterization of TADF NPs. Due to the poor water solubility of TADF molecules, to improve their bioavailability, water-dispersible TADF NPs were fabricated *via* a traditional nanoprecipitation method. As illustrated in **Figure 2a**, An-TPA NPs and An-Cz-Ph NPs were prepared by self-assembly for two-photon activated cellular fluorescence imaging (TPA imaging) and mitochondria-specific ROS production. **Figures 2b, f and 2c, g** display respectively SEM and TEM images of the An-TPA NPs and the An-Cz-Ph NPs, uncovering their monodispersed and well-defined spherical morphologies of ~ 80-90 nm in diameters. Corresponding hydrodynamic diameters of the An-TPA NPs and the An-Cz-Ph NPs were determined to be 78.1 and 93.3 nm by DLS measurements (**Figures 2d, h**). The small size below 100 nm of the two TADF NPs is not only beneficial for their uptake in tumor cells, but also in favor of the efficient accumulation at the tumor sites due to the enhanced permeability and retention (EPR) effect in future *in vivo* study, which

would greatly boost their practical PDT and fluorescence imaging. Both samples have PDI values below 0.2 suggesting their excellent monodispersibility. Besides, the as-prepared NPs also show good water-dispersibility (Insets of **Figures 2d, h**).

We also measured absorption and emission spectra of the free TADF molecules dissolved in tetrahydrofuran (THF) and the TADF NPs dispersed in deionized water respectively. As depicted in **Figures 2e, i**, the normalized absorbance profiles (dotted lines) of both TADF NPs exhibit a range of 200-600 nm with a red-shift of ~20-30 nm at the absorption edges comparing to that of their corresponding free TADF molecules, which are attributed to the strong intermolecular π-π interactions within the TADF NPs. Insets of **Figures 2e, i** are respectively photographs of the An-TPA or An-Cz-Ph molecules dissolved in THF (left) and the An-TPA or An-Cz-Ph NPs dispersed in deionized water under UV light (right), showing that TADF NPs display an obvious red or orange emission. Interestingly, compare with the An-Cz-Ph, the An-TPA is a typical aggregation-induced emission (AIE) based molecule with a flexible TPA group, leading to strong non-radiative transition *via* molecular vibration in solvent. Therefore, the An-TPA compound is non-emissive in THF but become highly emissive upon NP formation because the restriction of intramolecular rotations, which is in favor of the bioimaging application of the as-prepared TADF NPs. Moreover, the photoluminescence quantum yield (PLQY) of the An-TPA and An-Cz-Ph NPs dispersed in water were respectively determined to be ~3.7% and ~0.8% by an absolute method using a fluorescence spectrometer (FLS920P, Edinburgh Instruments) equipped with an integrating sphere. The higher PLQY of the An-TPA NPs might contribute to a lower singlet oxygen quantum yield since fluorescence emission competes with the singlet oxygen generation through intersystem crossing upon photo-excitation.

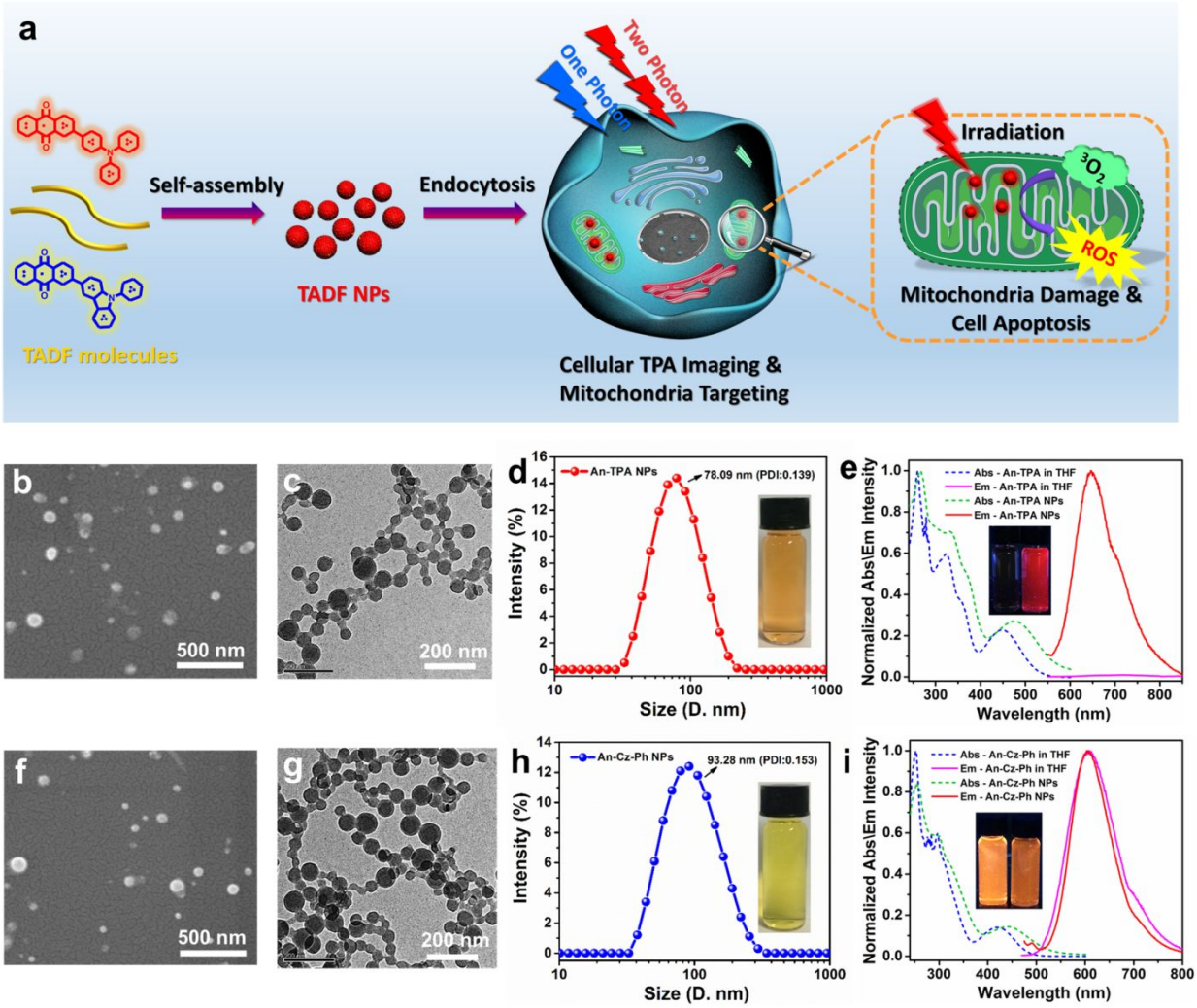

Figure 2. a) Schematic illustration of preparing the TADF NPs by self-assembly for two-photon activated cellular fluorescence imaging (TPA imaging) and mitochondria-specific ROS production; SEM images and corresponding TEM images of the An-TPA NPs (b, c) and An-Cz-Ph NPs (f, g); Dynamic light scattering (DLS) and polydispersity index (PDI) measurement of the d) An-TPA NPs and h) An-Cz-Ph NPs (The insets are photographs of the TADF NPs dispersed in deionized water under room light); e) Normalized absorbance and fluorescence spectra of free An-TPA molecules in THF and An-TPA NPs dispersion in water respectively (The insets are corresponding photographs of the An-TPA molecules (left) and the An-TPA NPs dispersion under UV light (right)); i) Normalized absorbance and fluorescence spectra of free An-Cz-Ph molecules in THF and An-Cz-Ph NPs dispersion in water respectively (The insets are corresponding photographs of the An-Cz-Ph molecules (left) and the An-Cz-Ph NPs dispersion under UV light (right))

2.3. Single-photon excited (SPE) and two-photon excited (TPE) cellular imaging of the TADF NPs. Two-photon activated PDT has been recently proposed to expand the PDT's biomedical applications, wherein two NIR photons instead of one visible photon are applied for PS excitation.[28–31] Penetration depth of the commonly applied visible light is very low while two-photon activated PDT exhibits not only better penetration depth but also spatial selectivity. To investigate the cellular imaging capability of the TADF NPs, both single-photon excited (SPE) and two-photon excited (TPE) fluorescence imaging were conducted individually with fluorescence microscopy as well as confocal laser scanning microscopy (CLSM) in A549 cell. For the SPE fluorescence imaging experiments, TADF NPs were excited at 380-420 nm. As exhibited in **Figure 3**, intense red fluorescence from both An-TPA and An-Cz-Ph NPs in cytoplasm were clearly detected. Additionally, CLSM Z-stack scanning mode images from the top to the bottom of A549 cell incubated with these NPs as shown in **Figure S4**, demonstrating that the TADF NPs can be successfully taken up into the cells rather than just being attached on the surfaces of cancer cells.

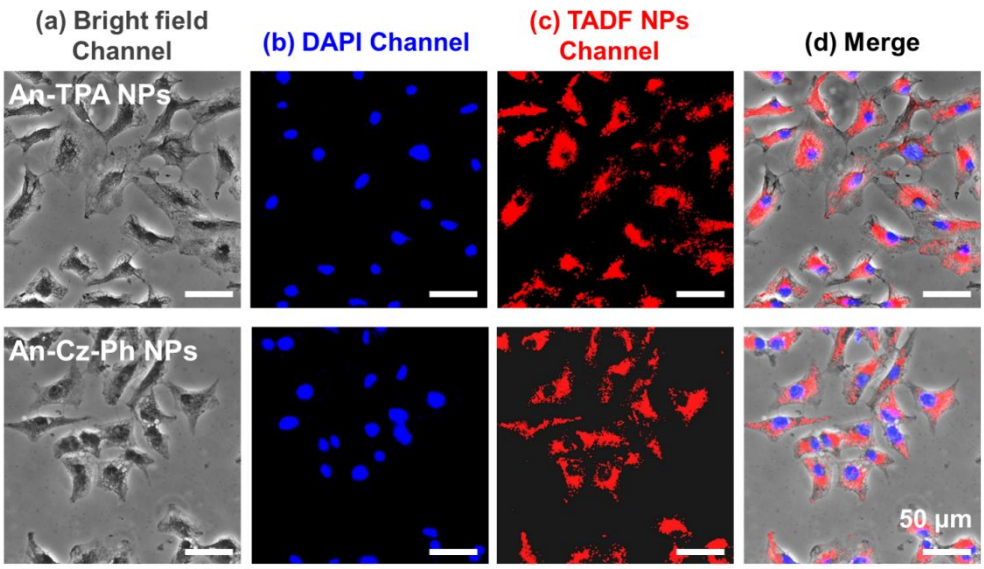

Figure 3. Single-photon excited (SPE) cellular imaging of the TADF NPs in A549 human lung cancer cells, detected by fluorescence microscopy. (a) Bright field channel; (b) DAPI channel (excitation wavelength: 330-380 nm); (c) TADF NPs channel (excitation wavelength: 380-420 nm); (d) Merge channel. Scale bar is 50 μm. Upper: An-TPA NPs group; Lower: the An-Cz-Ph NPs group.

Next, before the TPE cellular imaging experiments, two-photon optical properties of the as-prepared TADF NPs were evaluated by using a femtosecond (fs) laser pulse. The log-log plots of the detected TPE fluorescence emission intensity of the An-TPA NPs (**Figure 4a**) and the An-Cz-Ph NPs (**Figure 4c**) versus the excitation laser power intensity displayed slopes of 1.85 and 1.93 respectively. These near quadratic relationship between TPE emission intensity and input 800 nm excitation laser power firstly certified the TPE nature of the TADF NPs. Furthermore, the two-photon processes were also confirmed by the strong two-photon fluorescence of the TADF NPs at an excitation wavelength of 800 nm. TPE fluorescence spectra of the An-TPA NPs (**Figure 4b**) and the An-Cz-Ph NPs (**Figure 4d**) are respectively similar to that of their corresponding SPE fluorescence spectra (**Figures 2e, i**). Apart from 800 nm fs laser excitation, the two-photon characteristics of the TADF NPs were also demonstrated under excitation with an 880 nm fs laser (**Figure S5**).

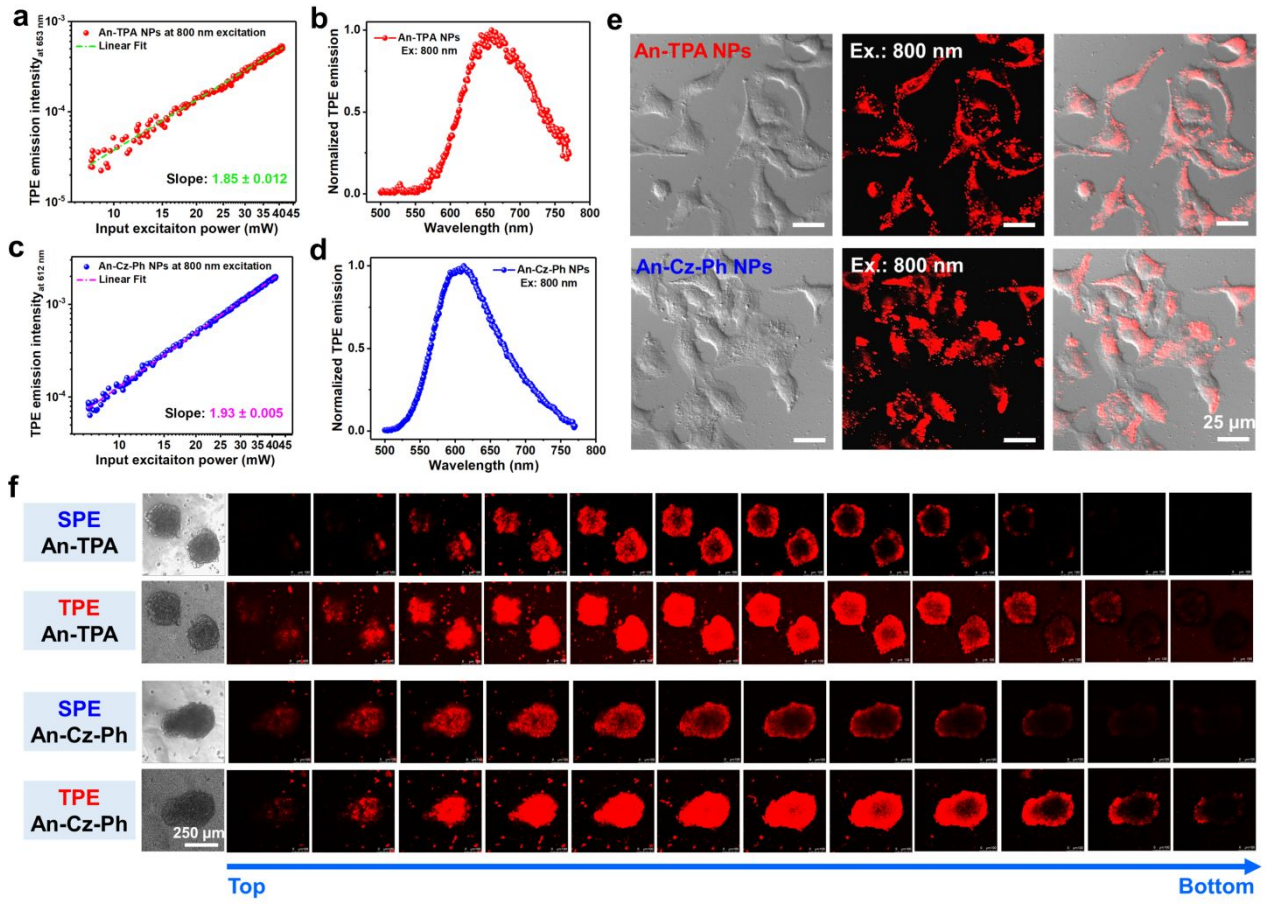

Figure 4. Input excitation power dependence curves of two-photon excited (TPE) emission intensity at a) 653 nm of An-TPA NPs and c) 612 nm of An-Cz-Ph NPs under 800 nm fs excitation; The corresponding normalized TPE emission spectra of b) An-TPA NPs and d) An-Cz-Ph NPs under 800 nm fs excitation; e) Cellular TPE CLSM images of the TADF NPs, monitored with excitation wavelength of 800 nm in A549 human lung cancer cells; f) SPE and TPE Z-stack CLSM images of A549 3D multicellular tumor spheroids (MCTSs) treated with An-TPA NPs and An-Cz-Ph NPs.

After confirming their two-photon properties, cellular TPE CLSM images of the TADF NPs were acquired under excitation at 880 nm fs laser in A549 cells. As exhibited in **Figure 4e**, strong red signals can be detected in cells after incubation with both An-TPA NPs and the An-Cz-Ph NPs. To further prove the superiority of the TPE fluorescence imaging, SPE and TPE Z-stack CLSM images of A549 3D multicellular tumor spheroids (MCTSs) respectively treated with An-TPA NPs and An-Cz-Ph NPs were captured. It has been well-documented that the heterogeneous 3D MCTSs,

exhibiting similar histological characteristics to the solid tumor nidus, have commonly been used to assess the performance of nano-biomaterials. As shown in **Figure 4f**, compared with the SPE images, the TPE-based Z-stack imaging modes displayed deeper penetration depths in A549 MCTS incubated with either An-TPA NPs or An-Cz-Ph NPs, owing to the long two-photon excitation wavelength at 800 nm. While in the case of the SPE modes, only the periphery of the MCTS exhibited relatively strong fluorescence at a much lower penetration depth. The corresponding quantifications of TADF fluorescence intensities further confirmed these results (**Figure S6**).

2.4. Singlet oxygen generation ability. To evaluate the $^1O_2$ generation ability of the water-dispersible TADF NPs, we employed the disodium salt of 9,10-anthracenedipropionicacid (ADPA) as a water-soluble $^1O_2$ sensor by recording the absorption degradation at 378 nm upon exposure to $^1O_2$. Time-dependent loss of ADPA absorption caused by the An-TPA NPs, the An-Cz-Ph NPs and DI water were respectively illustrated in **Figures 5a-c**. **Figure 5d** summarizes the bleaching results in ADPA absorption at 378 nm of different groups as a function of the light exposure time. Both the An-TPA NPs and the An-Cz-Ph NPs clearly displays that as the irradiation duration increases, absorption intensities of ADPA decrease significantly while the control group (only ADPA incubated in DI water without TADF NPs) shows negligible bleaching of ADPA. These results prove that the two TADF NPs are potential PS for PDT. Subsequently, we measured the $^1O_2$ quantum yield of the TADF NPs by using the ADPA as the $^1O_2$ sensing agent and a conventional PS Rose Bengal ($^1O_2$ quantum yield = 75% in water) as the standard reference. As presented in **Figure S7**, the An-TPA NPs and the An-Cz-Ph NPs dispersions exhibited high $^1O_2$ quantum yield which determined to be 22 % and 52 %, respectively. These yields are much higher than that of our

previously reported TADF NPs (10-15%[21]). Particularly, apart from an efficient ISC process, lifetime of triplet-excited state of the PS is also crucial to the formation of $^1O_2$. In our work, we have verified that the lifetime of An-TPA is much longer than that of An-Cz-Ph (1.3 vs 2.4 μs shown in **Figure S2**). Therefore, the exciton populating time in triplet-excited state of An-TPA is much longer than that in An-Cz-Ph, implying that the oxygen molecules at group state have higher probability to interact with triplet exciton of An-TPA for higher singlet oxygen quantum yield.

Moreover, the cellular $^1O_2$ generation abilities of the TADF NPs were further evidenced by CLSM images of live A549 cells treated with different groups, where 2,7-dichlorofluorescein diacetate (DCFH-DA) was used as the ROS indicator which would emit the green fluorescence in the presence of endogenous ROS (**Figure 5e**). Live A549 cells were pretreated with the An-TPA NPs or the An-Cz-Ph NPs and incubated with DCFH-DA. Before light irradiation, the cells show only red fluorescence from the NPs and green signal from ROS can only be observed after irradiation confirming intracellular generation of $^1O_2$.

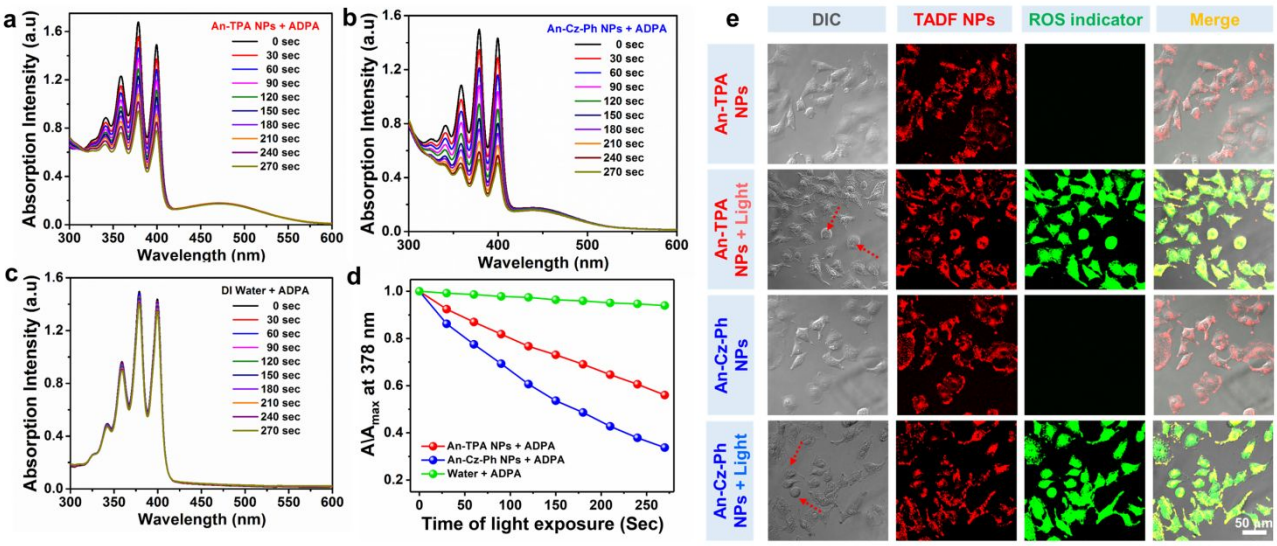

Figure 5. Time-dependent degradation of ADPA absorption induced by $^1O_2$ generated by a) the An-TPA NPs, b) the An-Cz-Ph NPs and c) DI water; d) Loss in ADPA absorption at 378 nm with various light exposure duration; e)

Intracellular ROS analysis by CLSM images of live A549 human lung cancer cells treated with different groups (Ex: 488 nm; Em: 640-660 nm for TADF NPs; 510-525 nm for ROS indicator).

2.5. Cancer-mitochondria-targeting capabilities. To optimize the efficacy of PDT, subcellular targeting strategy has drawn extensive attention in PDT treatment since it enables the PSs to target specific subcellular organelles such as nuclei,[32,33] lysosomes,[34,35] plasma membrane[36,37] and mitochondria[38–41] which are more vulnerable to ROSs. Most particularly, mitochondria which are the "powerhouse" of the cell, have been recognized as a promising therapeutic target for highly efficient PDT cancer treatment. As one of the most crucial subcellular organelles in organisms, mitochondria undertake various critical biological functions in cells, including energy supply, redox status maintenance and molecular metabolism.[40] Mitochondrial dysfunction could induce mitochondria-mediated apoptosis. Thus, producing $^1O_2$ inside mitochondria can directly damage them and maximize the cytotoxic effect in PDT treatment.

To demonstrate the efficient mitochondria-targeting capabilities of the as-prepared TADF NPs, we firstly investigated the intracellular colocalization of the two TADF NPs with a commercial mitochondrion-staining agent MitoTracker Green and a lysosome-staining agent LysoTracker Green in A549 cancer cells, respectively. As shown in **Figure 6**, in the merge channels, it is found that the red signals from the TADF NPs merges well with the green fluorescence from MitoTracker. However, in the case of lysosome co-localization images, these two signals exhibited poor overlap. Furthermore, the Pearson's colocalization coefficients which is used to assess the overlap efficiency between the TADF NPs' red emission and MitoTracker's or LysoTracker's green emission, are calculated to be above 0.9 (0.93 for the An-TPA NPs, 0.95 for the An-Cz-Ph NPs) and 0.5 (0.55 for the An-TPA NPs, 0.53 for the An-Cz-Ph NPs), respectively. The corresponding fluorescence

topographic profiles displaying the fluorescence intensity along the white lines marked in TADF NP channel (red) and organelle-tracker channel (green), further indicate that fluorescence of the TADF NPs overlap well with that of MitoTracker instead of LysoTracker. Meanwhile, we propose the possible reason why the TADF NPs show preferable mitochondria-targeting properties is probably because of the high lipophilicity stemming from the five phenyl groups in their molecular structures.[42]

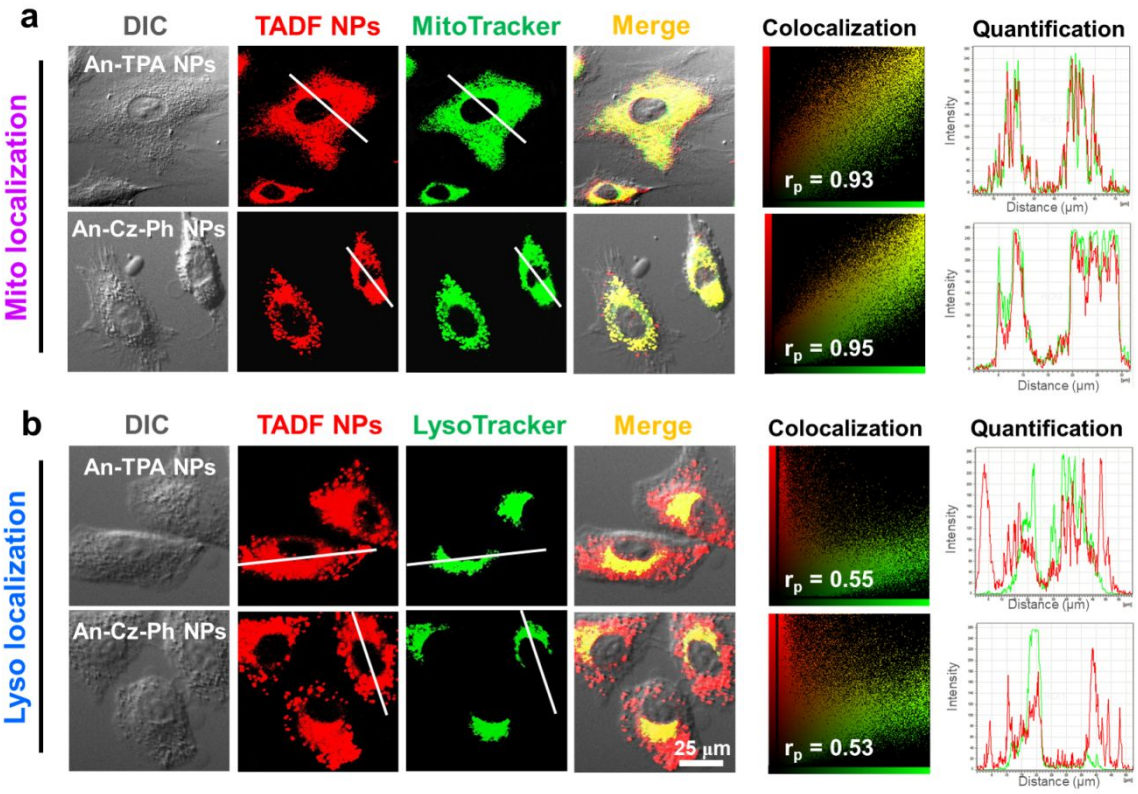

Figure 6. a) Representative mitochondria co-localization images of the An-TPA NPs and the An-Cz-Ph NPs by CLSM in A549 human lung cancer cells, where r_p indicates Pearson's colocalization coefficient; d) Representative lysosome co-localization images of the An-TPA NPs and the An-Cz-Ph NPs by CLSM in A549 cells, where r_p indicates Pearson's colocalization coefficient. Fluorescence topographic profiles display fluorescence intensity along the white lines marked in TADF NP channel (red) and organelle-tracker channel (green), respectively.

Subsequently, to further investigate their cancer-mitochondria-targeting capabilities, we compared the intracellular mitochondrial localization of the TADF NPs in two cancer cell lines (A549 or Hela cancer cells) and two normal cell lines (NIH 3T3 or MCR-5 normal cells). As exhibited in **Figure 7**, for both A549 and Hela cells, confocal microscopy analysis indicates that the red fluorescence signals are well-overlapped with the green signals from the MitoTracker Green. It is interesting, the mitochondrial targeting characteristic of the two NPs are much less obvious in the two normal cell lines (**Figures 7c and d**). Particularly, we also observed that while almost all NPs are successfully internalized into the cancer cells, the uptake in normal cells appears to be much less effective as indicated by the red fluorescence outside the cells (marked with white dashed regions in figures 7c and d). Therefore, the mitochondria targeting ability of the TADF NPs is dependent on cell type in which the TADF NPs exhibit better selectivity for mitochondria in cancer cells compared to normal cells, showing great promise as a powerful tool for PDT in cancer treatments. Meanwhile, the cancer-mitochondria-targeting mechanisms of these TADF NPs should be further systematically studied and clarified in future works.

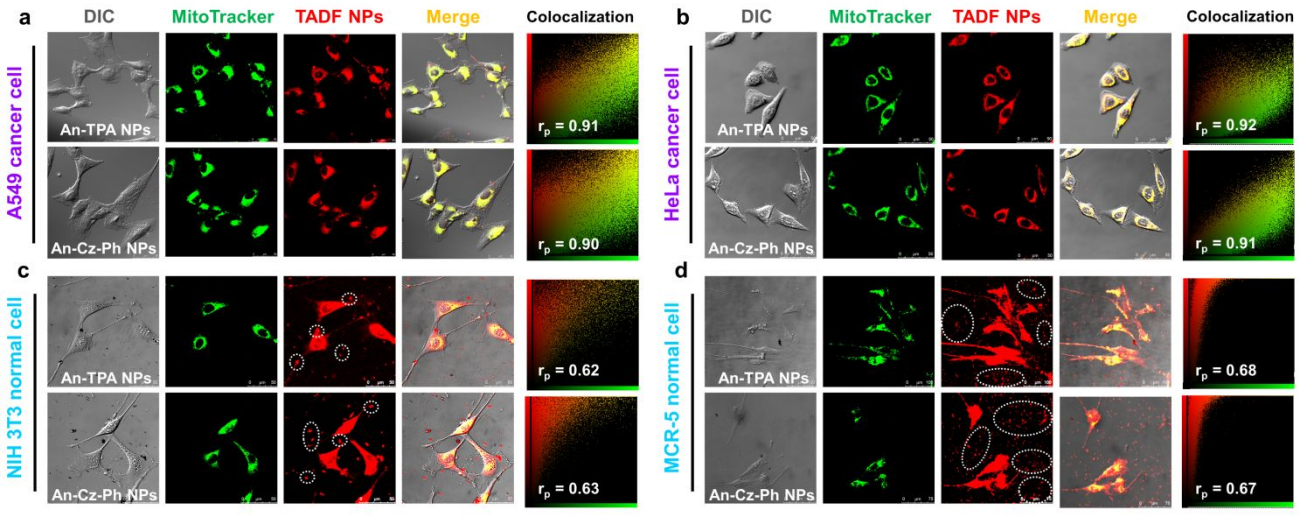

Figure 7. Representative mitochondria colocalization images of the An-TPA NPs and the An-Cz-Ph NPs by CLSM

in cancer cells (A549 or Hela cancer cells) and normal cells (NIH 3T3 or MCR-5 normal cells).

2.6. Mitochondrial dysfunction and *in vitro* cytotoxicities by PDT. It has been mentioned above that PDT effect on mitochondria would cause mitochondrial dysfunction as well as lead to cell apoptosis. Loss of mitochondrial membrane potential (MMP) is a typical characteristic of mitochondrial damage. Therefore, to monitor the mitochondrial dysfunction in cancer cells, a membrane-permeable JC-1 dye was selected to evaluate the MMP changes. As described in **Figure 8a**, JC-1 dye can undergo a reversible fluorescence change between its aggregate (red; healthy cells with high MMP) and monomer (green; apoptotic cells with low MMP) states to observe the mitochondrial depolarization process. Representative CLSM images of JC-1 stained A549 cells after different treatments are shown in **Figure 8b**. Obviously, in the TADF NPs incubated cells, the green fluorescence signals increased while the red fluorescence signals decreased upon light irradiation, demonstrating that the generated ROS would induce the loss of MMP and dysfunction of mitochondria. In contrast, only light irradiation without NPs as well as the uptake of TADF NPs in mitochondria darkly do not depolarize the mitochondrial membrane, as proved by the weak green signals and intense red signals of JC-1 dye. These results further suggested the mitochondria targeting ability of the as-fabricated TADF NPs which can induce mitochondria-mediated apoptosis.

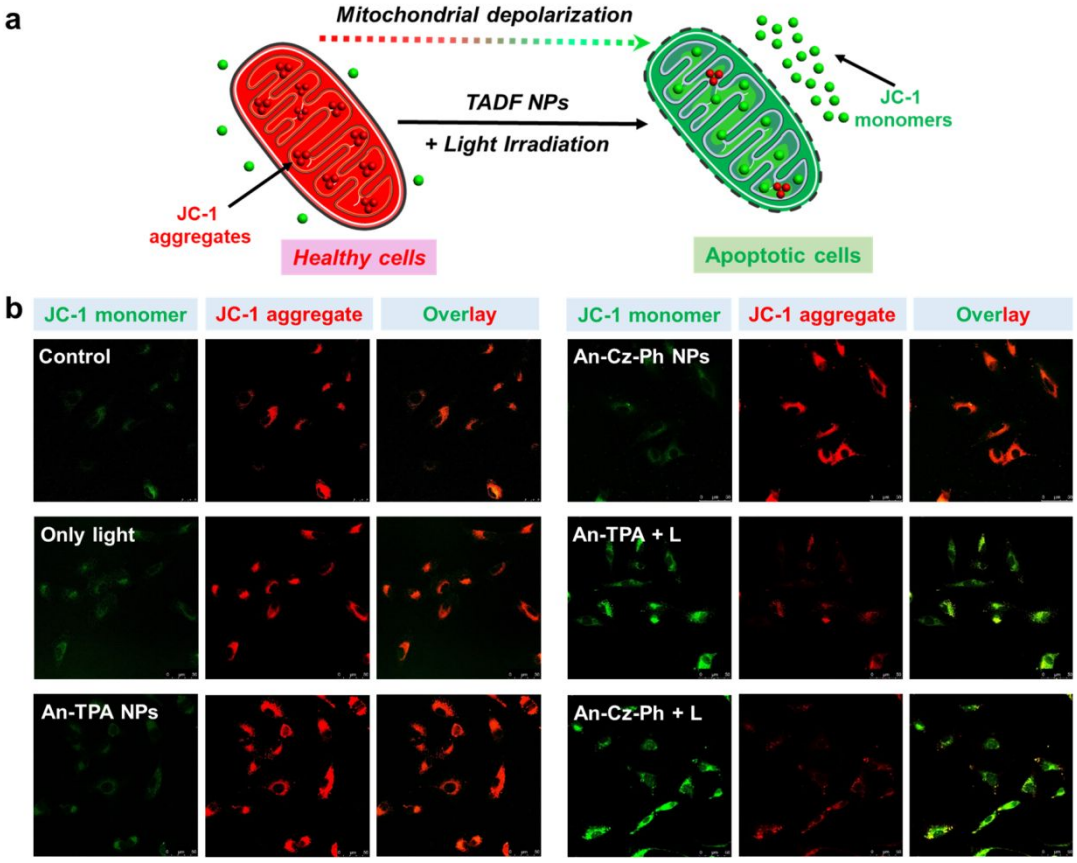

Figure 8. a) Schematic illustration of a membrane-permeable JC-1 dye to observe mitochondrial depolarization where JC-1 dye exhibits reversible fluorescence between its aggregate (red; healthy cells) and monomer (green; apoptotic cells) states; b) CLSM images of JC-1 stained A549 cells after different treatments. The increase of green fluorescence in the light irradiated cells added TADF NPs indicated a loss of mitochondrial membrane potential (MMP).

Finally, we measured the *in vitro* cytotoxicities of the An-TPA NPs and the An-Cz-Ph NPs with or without an ultralow intensity white light irradiation (28 mW/cm^2 for 5 min) by using MTT assay. As presented in **Figures 9a, b**, the two TADF NPs show dose-dependent cytotoxicities while both NPs without light (pink and blue columns) and the only light group exhibit low toxicities. The excellent cancer-cell-killing abilities at such low concertation and upon such ultralow irradiance are attributed to the high $^1O_2$ quantum yield as well as good mitochondria-specific ROS production. In addition, to

further track the cytotoxic effect induced by TPE irradiation, morphology changes of live A549 cells were observed by CLSM under TPE excitation with an 880 nm fs laser. As shown in **Figure 9c**, with the irradiation time extended from 0 to 15 min, the morphology of live A549 cells pretreated with the TADF NPs changed dramatically where cell shrinkage and numerous blebs were notably found. For comparison, the cells without NPs exhibit negligible change under the same laser irradiation.

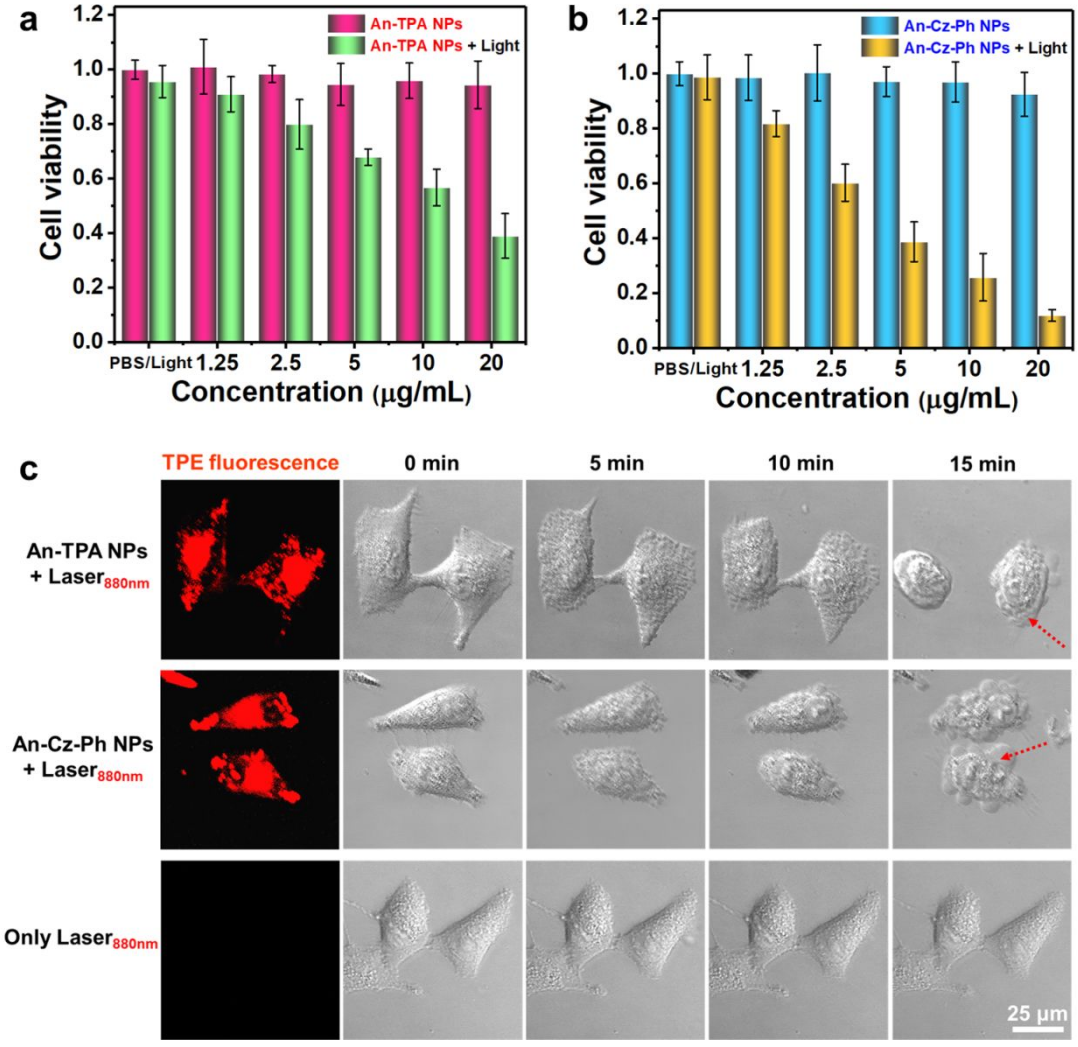

Figure 9. *In vitro* cytotoxicity of a) the An-TPA NPs and b) the An-Cz-Ph NPs with or without white light irradiation (28 mW/cm^2 for 5 min); c) TPE fluorescence images of A549 cells with or without TADF NPs, and the corresponding bright field, time-dependent (0-15 min) CLSM images. The red dotted arrows indicate membrane blebs.

4. CONCLUSION

In conclusion, for the first time, we developed two intrinsically cancer-mitochondria-targeted TADF NPs for two-photon activated fluorescence imaging and PDT. The as-prepared TADF NPs provided following merits: 1) satisfactory $^1O_2$ quantum yield from 22% to 52%, which are much higher than that of previously reported TADF NPs (10-15%); 2) sufficient light penetration depth due to two-photon activation to boost the fluorescence imaging as well as PDT performances; 3) excellent intrinsically mitochondria targeting capabilities without the need of extra chemical or physical modifications, induced a mitochondria-mediated apoptosis; meanwhile, these two TADF NPs also exhibited better selectivity for mitochondria in cancer cells compared to normal cells, showing great promise as a powerful tool for PDT; 4) remarkable cancer-cell-killing abilities upon an ultralow white light irradiance as well as two-photon activated excitation with an 880 nm fs laser. Besides, since the TADF NPs can cause mitochondria dysfunction which would be potentially used to induce immunogenic cell death, the TADF NPs would also be explored to achieve synergistic therapeutic outcome integrating PDT with cancer immunotherapy in our future study. Nevertheless, the intrinsically cancer-mitochondria-targeting mechanisms as well as surface modification for further functionalization should be further systematically studied in our future works. All in all, we believe such multifunctional TADF NPs based on a single molecule will open new opportunities for the development of novel PDT agents for cancer diagnosis and therapy.

ASSOCIATED CONTENT

Supporting Information. Description of materials and methods and Supporting Figures: (Figure S1) Photographs of the An-TPA powder, An-Cz-Ph powder and the FITC powder taken under room light (upper row) and UV light (lower row), (Figure S2) Steady-state fluorescence spectra, phosphorescence spectra and fluorescence lifetime of An-TPA and An-Cz-Ph, (Figure S3) Steady-state fluorescence spectra, phosphorescence spectra and fluorescence lifetime of An-TPA and An-Cz-Ph, (Figure S4) CLSM Z-stack scanning mode images of A549 cell incubated with the An-TPA NPs and An-Cz-Ph NPs, (Figure S5) Input excitation power dependence of TPE emission intensity and the normalized TPE emission spectra of An-TPA NPs and An-Cz-Ph NPs under 880 nm fs excitation, (Figure S6) The mean fluorescence intensities of SPE and TPE Z-stack CLSM images of A549 3D MCTSs, (Figure S7) Chemical trapping measurements of the $^1O_2$ quantum yield. This material is available free of charge *via* the Internet at http://pubs.acs.org.

AUTHOR INFORMATION

Corresponding Author

* E-mail: lishengliang@iccas.ac.cn

* E-mail: apcslee@cityu.edu.hk

ORCID

Chun-Sing Lee: 0000-0001-6557-453X

Shengliang Li: 0000-0002-3890-8482

Jinfeng Zhang: 0000-0002-1899-888X

Wen-Cheng Chen: 0000-0003-3788-3516

Notes

The authors declare no competing financial interest.

ACKNOWLEDGMENT

C.S.L. would like to thank financial support by City University of Hong Kong (CityU Internal Funds for External Grant Schemes Project No. 9678157 and CityU Applied Research Grant Project no. 9667160). J.Z. would like to acknowledge financial support by Beijing Institute of Technology Research Fund Program for Young Scholars and the National Natural Science Foundation of China (Project No. 91859123).

REFERENCES

[1] Castano, A. P.; Mroz, P.; Hamblin, M. R. Photodynamic Therapy and Anti-Tumour Immunity. *Nat. Rev. Cancer* ***2006***, *6*, 535–545.

[2] Lovell, J. F.; Liu, T. W. B.; Chen, J.; Zheng, G. Activatable Photosensitizers for Imaging and Therapy. *Chem. Rev.* **2010**, *110*, 2839–2857.

[3] Lucky, S. S.; Soo, K. C.; Zhang, Y. Nanoparticles in Photodynamic Therapy. *Chem. Rev.* **2015**, *115*, 1990–2042.

[4] Zhang, J.; Liang, Y.-C.; Lin, X.; Zhu, X.; Yan, L.; Li, S.; Yang, X.; Zhu, G.; Rogach, A. L.; Yu, P. K. N.; Shi, P.; Tu, L. C.; Chang, C. C.; Zhang, X.; Chen, X.; Zhang, W.; Lee, C. S. Self-Monitoring and Self-Delivery of Photosensitizer-Doped Nanoparticles for Highly Effective Combination Cancer Therapy *in Vitro* and *in Vivo*. *ACS Nano* **2015**, *9*, 9741–9756.

[5] Li J.; Pu K. Development of Organic Semiconducting Materials for Deep-Tissue Optical Imaging, Phototherapy and Photoactivation. *Chem. Soc. Rev.* **2019**, *48*, 38-71.

[6] Jiang Y.; Pu K. Multimodal Biophotonics of Semiconducting Polymer Nanoparticles. *Acc. Chem. Res.* **2018**, *51*, 1840-1849.

[7] Cui D.; Huang J.; Zhen X.; Li J.; Jiang Y.; Pu K. A Semiconducting Polymer Nano-prodrug for Hypoxia-Activated Photodynamic Cancer Therapy. *Angew. Chem. Inter. Ed.* **2019**, *58*, 5920.

[8] Zhu H.; Li J.; Qi X.; Chen P.; Pu K. Oxygenic Hybrid Semiconducting Nanoparticles for Enhanced Photodynamic Therapy. *Nano Lett.* **2018**, *18*, 586-594.

[9] Li, J.; Huang, J.; Lyu, Y.; Huang, J.; Jiang,Y.; Xie, C.; Pu. K. Photoactivatable Organic Semiconducting Pro-nanoenzymes. *J. Am. Chem. Soc.* **2019**, *141*, 4073-4079.

[10] Xu, S.; Yuan, Y.; Cai, X.; Zhang, C.-J.; Hu, F.; Liang, J.; Zhang, G.; Zhang, D.; Liu, B. Tuning the Singlet-Triplet Energy Gap: A Unique Approach to Efficient Photosensitizers with Aggregation-Induced Emission (AIE) Characteristics. *Chem. Sci.* **2015**, *6*, 5824–5830.

[11] Guo, Z.; Zou, Y.; He, H.; Rao, J.; Ji, S.; Cui, X.; Ke, H.; Deng, Y.; Yang, H.; Chen, C.; Zhao, Y.; Chen, H. Bifunctional Platinated Nanoparticles for Photoinduced Tumor Ablation. *Adv. Mater.* **2016**, *28*, 10155–10164.

[12] Wang, D.; Lee, M. M. S.; Shan, G.; Kwok, R. T. K.; Lam, J. W. Y.; Su, H.; Cai, Y.; Tang, B. Z. Highly Efficient Photosensitizers with Far-Red/Near-Infrared Aggregation-Induced Emission for In Vitro and In Vivo Cancer Theranostics. *Adv. Mater.* **2018**, *30*, 1802105.

[13] Wu, W.; Mao, D.; Xu, S.; Kenry; Hu, F.; Li, X.; Kong, D.; Liu, B. Polymerization-Enhanced Photosensitization. *Chem* **2018**, *4*, 1937–1951.

[14] Chi, Y.; Chou, P.-T. Transition-Metal Phosphors with Cyclometalating Ligands: Fundamentals and Applications. *Chem. Soc. Rev.* **2010**, *39*, 638–655.

[15] Zhao, J.; Wu, W.; Sun, J.; Guo, S. Triplet Photosensitizers: From Molecular Design to Applications. *Chem. Soc. Rev.* **2013**, *42*, 5323–5351.

[16] Jiang, X.; Peng, J.; Wang, J.; Guo, X.; Zhao, D.; Ma, Y. Iridium-Based High-Sensitivity Oxygen

Sensors and Photosensitizers with Ultralong Triplet Lifetimes. *ACS Appl. Mater. Interfaces* **2016**, *8*, 3591–3600.

[17] Stohs, S. J.; Bagchi, D. Oxidative Mechanisms in the Toxicity of Metal Ions. *Free Radic. Biol. Med.* **1995**, *18*, 321–336.

[18] Lim, S. H.; Thivierge, C.; Nowak-Sliwinska, P.; Han, J.; van den Bergh, H.; Wagnières, G.; Burgess, K.; Lee, H. B. In Vitro and in Vivo Photocytotoxicity of Boron Dipyrromethene Derivatives for Photodynamic Therapy. *J. Med. Chem.* **2010**, *53*, 2865–2874.

[19] Uoyama, H.; Goushi, K.; Shizu, K.; Nomura, H.; Adachi, C. Highly Efficient Organic Light-Emitting Diodes from Delayed Fluorescence. *Nature* **2012**, *492*, 234–238.

[20] Goushi, K.; Yoshida, K.; Sato, K.; Adachi, C. Organic Light-Emitting Diodes Employing Efficient Reverse Intersystem Crossing for Triplet-to-Singlet State Conversion. *Nat. Photonics* **2012**, *6*, 253–258.

[21] Liu, X.-K.; Chen, Z.; Zheng, C.-J.; Liu, C.-L.; Lee, C.-S.; Li, F.; Ou, X.-M.; Zhang, X.-H. Prediction and Design of Efficient Exciplex Emitters for High-Efficiency, Thermally Activated Delayed-Fluorescence Organic Light-Emitting Diodes. *Adv. Mater.* **2015**, *27*, 2378–2383.

[22] Liu, X.-K.; Chen, Z.; Qing, J.; Zhang, W.-J.; Wu, B.; Tam, H. L.; Zhu, F.; Zhang, X.-H.; Lee, C.-S. Remanagement of Singlet and Triplet Excitons in Single-Emissive-Layer Hybrid White Organic Light-Emitting Devices Using Thermally Activated Delayed Fluorescent Blue Exciplex. *Adv. Mater.* **2015**, *27*, 7079–7085.

[23] Xiong, X.; Song, F.; Wang, J.; Zhang, Y.; Xue, Y.; Sun, L.; Jiang, N.; Gao, P.; Tian, L.; Peng, X. Thermally Activated Delayed Fluorescence of Fluorescein Derivative for Time-Resolved and Confocal Fluorescence Imaging. *J. Am. Chem. Soc.* **2014**, *136*, 9590–9597.

[24] Li, T.; Yang, D.; Zhai, L.; Wang, S.; Zhao, B.; Fu, N.; Wang, L.; Tao, Y.; Huang, W. Thermally Activated Delayed Fluorescence Organic Dots (TADF Odots) for Time-Resolved and Confocal Fluorescence Imaging in Living Cells and In Vivo. *Adv. Sci.* **2017**, *4*, 1600166–1600176.

[25] Zhu, Z.; Tian, D.; Gao, P.; Wang, K.; Li, Y.; Shu, X.; Zhu, J.; Zhao, Q. Cell-Penetrating Peptides Transport Noncovalently Linked Thermally Activated Delayed Fluorescence Nanoparticles for Time-Resolved Luminescence Imaging. *J. Am. Chem. Soc.* **2018**, *140*, 17484–17491.

[26] Zhang, J.; Chen, W.; Chen, R.; Liu, X.-K.; Xiong, Y.; Kershaw, S. V.; Rogach, A. L.; Adachi, C.; Zhang, X.; Lee, C.-S. Organic Nanostructures of Thermally Activated Delayed Fluorescent Emitters with Enhanced Intersystem Crossing as Novel Metal-Free Photosensitizers. *Chem. Commun.* **2016**, *52*, 11744–11747.

[27] Y. J. Shiu, Y. C. Cheng, W. L. Tsai, C. C. Wu, C. T. Chao, C. W. Lu, Y. Chi, Y. T. Chen, S. H. Liu, P. T. Chou, Pyridyl Pyrrolide Boron Complexes: The Facile Generation of Thermally Activated Delayed Fluorescence And Preparation of Organic Light-Emitting Diodes. *Angew. Chem. Int. Ed.* **2016**, *55*, 3017–3021.

[28] Zhuang, X.; Ma, X.; Xue, X.; Jiang, Q.; Song, L.; Dai, L.; Zhang, C.; Jin, S.; Yang, K.; Ding, B.; Wang, P. C.; Liang, X. J. A Photosensitizer-Loaded DNA Origami Nanosystem for Photodynamic Therapy. *ACS Nano* **2016**, *10*, 3486–3495.

[29] Lan, M.; Zhao, S.; Xie, Y.; Zhao, J.; Guo, L.; Niu, G.; Li, Y.; Sun, H.; Zhang, H.; Liu, W.; Zhang, J.; Wang, P.; Zhang, W. Water-Soluble Polythiophene for Two-Photon Excitation Fluorescence Imaging and Photodynamic Therapy of Cancer. *ACS Appl. Mater. Interfaces* **2017**, *9*, 14590–14595.

[30] Cao, H.; Wang, L.; Yang, Y.; Li, J.; Qi, Y.; Li, Y.; Li, Y.; Wang, H.; Li, J. An Assembled Nanocomplex for Improving Both Therapeutic Efficiency and Treatment Depth in Photodynamic Therapy. *Angew. Chem., Int. Ed.* **2018**, *57*, 7759–7763.

[31] Gao, R.; Mei, X.; Yan, D.; Liang, R.; Wei, M. Nano-Photosensitizer Based on Layered Double Hydroxide and Isophthalic Acid for Singlet Oxygenation and Photodynamic Therapy. *Nat. Commun.* **2018**, *9*, 2798.

[32] Pan, L.; Liu, J.; Shi, J. Intranuclear Photosensitizer Delivery and Photosensitization for Enhanced Photodynamic Therapy with Ultralow Irradiance. *Adv. Funct. Mater.* **2014**, *24*, 7318–7327.

[33] Han, K.; Zhang, W.-Y.; Zhang, J.; Lei, Q.; Wang, S.-B.; Liu, J.-W.; Zhang, X.-Z.; Han, H.-Y. Acidity-Triggered Tumor-Targeted Chimeric Peptide for Enhanced Intra-Nuclear Photodynamic Therapy. *Adv. Funct. Mater.* **2016**, *26*, 4351–4361.

[34] Zhao, S.; Niu, G.; Wu, F.; Yan, L.; Zhang, H.; Zhao, J.; Zeng, L.; Lan, M. Lysosome-Targetable Polythiophene Nanoparticles for Two-Photon Excitation Photodynamic Therapy and Deep Tissue Imaging. *J. Mater. Chem. B* **2017**, *5*, 3651–3657.

[35] Zhang, D.-Y.; Zheng, Y.; Zhang, H.; He, L.; Tan, C.-P.; Sun, J.-H.; Zhang, W.; Peng, X.; Zhan, Q.; Ji, L.-N.; Mao, Z. W. Ruthenium Complex-Modified Carbon Nanodots for Lysosome-Targeted One- and Two-Photon Imaging and Photodynamic Therapy. *Nanoscale* **2017**, *9*, 18966–18976.

[36] Luo, G.-F.; Chen, W.-H.; Hong, S.; Cheng, Q.; Qiu, W.-X.; Zhang, X.-Z. A Self-Transformable pH-Driven Membrane-Anchoring Photosensitizer for Effective Photodynamic Therapy to Inhibit Tumor Growth and Metastasis. *Adv. Funct. Mater.* **2017**, *27*, 1702122–1702134.

[37] Jia, H.-R.; Jiang, Y.-W.; Zhu, Y.-X.; Li, Y.-H.; Wang, H.-Y.; Han, X.; Yu, Z.-W.; Gu, N.; Liu, P.; Chen, Z.; Wu, F. G. Plasma Membrane Activatable Polymeric Nanotheranostics with Self-Enhanced Light-Triggered Photosensitizer Cellular Influx for Photodynamic Cancer Therapy. *J. Control. Release* **2017**, *255*, 231–241.

[38] Tan, X.; Luo, S.; Long, L.; Wang, Y.; Wang, D.; Fang, S.; Ouyang, Q.; Su, Y.; Cheng, T.; Shi, C. Structure-Guided Design and Synthesis of a Mitochondria-Targeting Near-Infrared Fluorophore with Multimodal Therapeutic Activities. *Adv. Mater.* **2017**, *29*, 1704196–1704204.

[39] Jung, H. S.; Lee, J.-H.; Kim, K.; Koo, S.; Verwilst, P.; Sessler, J. L.; Kang, C.; Kim, J. S. A Mitochondria-Targeted Cryptocyanine-Based Photothermogenic Photosensitizer. *J. Am. Chem. Soc.* **2017**, *139*, 9972–9978.

[40] Ni, K.; Lan, G.; Veroneau, S. S.; Duan, X.; Song, Y.; Lin, W. Nanoscale Metal-Organic Frameworks for Mitochondria-Targeted Radiotherapy-Radiodynamic Therapy. *Nat. Commun.* **2018**, *9*, 4321.

[41] Yang, G.; Xu, L.; Xu, J.; Zhang, R.; Song, G.; Chao, Y.; Feng, L.; Han, F.; Dong, Z.; Li, B.; Liu, Z. Smart Nanoreactors for pH-Responsive Tumor Homing, Mitochondria-Targeting, and Enhanced Photodynamic-Immunotherapy of Cancer. *Nano Lett.* **2018**, *18*, 2475–2484.

[42] J. Morgan, A. R. Oseroff, Mitochondria-Based Photodynamic Anti-cancer therapy. *Adv. Drug Deliv. Rev.* **2001**, 49, 71–86.

Table of Contents Graphic